The Origin and Control of the Sources of AMR in (Ga,Mn)As Devices

A. W. Rushforth [a,*], K. Výborný [b], C. S. King [a], K. W. Edmonds [a], R. P. Campion [a], C. T. Foxon [a], J. Wunderlich [c], A. C. Irvine [d], V. Novák [b], K. Olejník [b], A. A. Kovalev [e], Jairo Sinova [e], T. Jungwirth [b,a], and B. L. Gallagher [a]

[a] *School of Physics and Astronomy, University of Nottingham, Nottingham NG7 2RD, UK*

[b] *Institute of Physics, Academy of Sciences of the Czech Republic, Cukrovarnická 10, 162 53 Praha 6, Czech Republic*

[c] *Hitachi Cambridge Laboratory, Cambridge CB3 0HE, UK*

[d] *Microelectronics Research Centre, Cavendish Laboratory, University of Cambridge, CB3 0HE, UK*

[e] *Department of Physics, Texas A&M University, College Station, TX 77843-4242, USA*

Abstract

We present details of our experimental and theoretical study of the components of the anisotropic magnetoresistance (AMR) in (Ga,Mn)As. We develop experimental methods to yield directly the non-crystalline and crystalline AMR components which are then independently analyzed. These methods are used to explore the unusual phenomenology of the AMR in ultra thin (5nm) (Ga,Mn)As layers and to demonstrate how the components of the AMR can be engineered through lithography induced local lattice relaxations. We expand on our previous [Phys. Rev. Lett. **99**, 147207 (2007)] theoretical analysis and numerical calculations to present a simplified analytical model for the origin of the non-crystalline AMR. We find that the sign of the non-crystalline AMR is determined by the form of spin-orbit coupling in the host band and by the relative strengths of the non-magnetic and magnetic contributions to the impurity potential.

Key words: AMR, anisotropic magnetoresistance, GaMnAs
PACS: 75.47.-m, 75.50.Pp, 75.70.Ak

1 Introduction

The Anisotropic Magnetoresistance (AMR) in ferromagnetic metals has been the subject of many studies since it was discovered more than a century ago[1]. The effect describes the change of the electrical resistance in response to a change in the orientation of the magnetization. Phenomenologically, AMR has a non-crystalline component, arising from the lower symmetry for a specific current direction, and crystalline components arising from the crystal symmetries [2,3]. In ferromagnetic metals the AMR components have been extracted indirectly from experimental data by fitting the total angular dependences [3]. The coefficients can be obtained by numerical *ab initio* transport calculations [4], but these have no clear connection to the standard physical model of transport arising from spin dependent scattering of current carrying low mass *s*-states into heavy-mass *d*-states [5].

In the dilute magnetic semiconductor (Ga,Mn)As, it has been observed that the AMR consists of a non-crystalline component of the opposite sign (compared to most ferromagnetic metals) and typically much weaker crystalline terms reflecting the underlying magnetocrystalline anisotropies [6,7,8,9,10,11,12]. In our recent work [13] we developed experimental methods to yield directly the non-crystalline and crystalline components of the AMR in (Ga,Mn)As. Numerical microscopic calculations were employed to calculate the AMR components, achieving good agreement with experimental results. An analytical model was introduced to explain the physical origin of the AMR terms, in particular to show that the sign of the non-crystalline term is determined by the ratio of the magnetic and non-magnetic components of the scattering potential. Here we expand our previous work to include details of that analytical model and a detailed explanation of how the components of the AMR can be separately extracted from the experimental data.

2 Experiment

25nm and 5nm $Ga_{0.95}Mn_{0.05}As$ films were grown by low temperature molecular beam epitaxy onto a 330nm HT-GaAs buffer layer grown on a semi-insulating GaAs(001) substrate. Standard photolithography techniques were used to fabricate two sets of Hall bars of width 45μm with voltage probes separated by 285μm, with the current along the [100], [010], [110] and [1$\bar{1}$0] directions. The longitudinal resistance R_{xx} and the Hall resistance R_{xy} were measured using four probe techniques with a DC current of 1μA. We also measured devices

* Corresponding author.
Email address: Andrew.rushforth@nottingham.ac.uk (A. W. Rushforth).

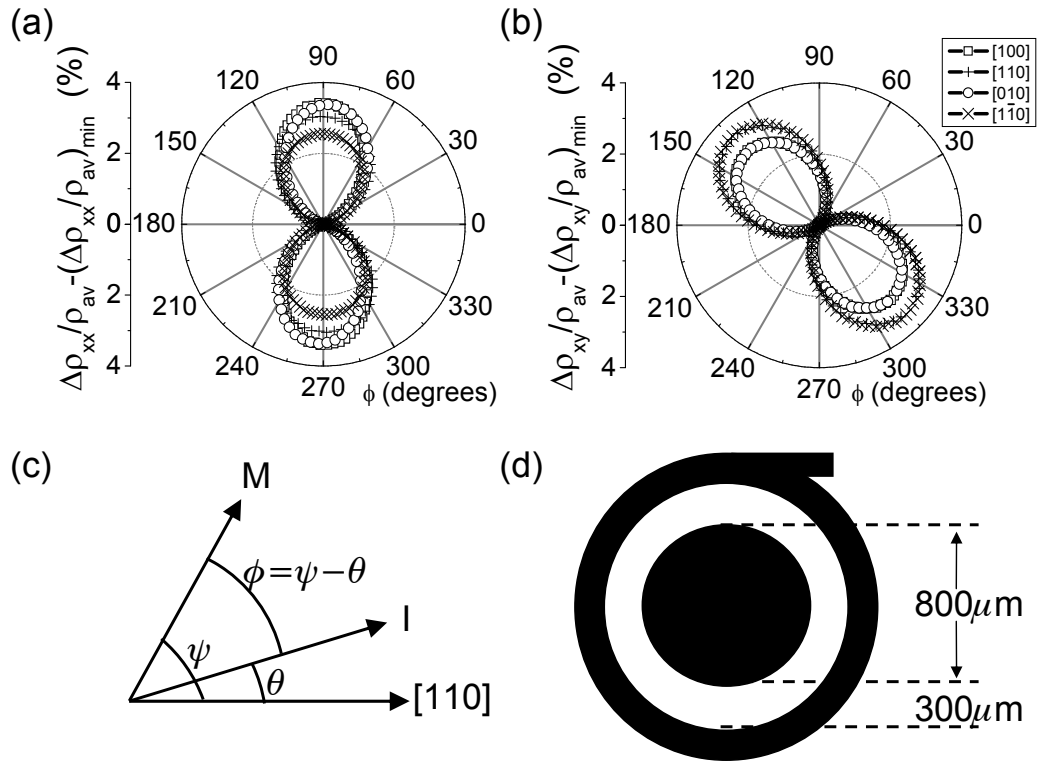

Fig. 1. (a) Measured (at 4.2 K) longitudinal and (b) transverse AMR for as-grown 25nm thick $Ga_{0.95}Mn_{0.05}As$ film as a function of the angle between magnetization in the plane of the film and the current. The legend shows the direction of the current. The y-axes show $\Delta\rho/\rho_{av}$ shifted so that the minimum is at zero, to show the symmetries present in the data more clearly. (c) Definition of the angles referred to in the text. (d) Corbino geometry.

with a Corbino geometry (Fig. 1(d)) in which the current flows radially in the plane of the material. All measurements were made on as-grown material (i.e. without annealing). Magnetoresistances were measured with a saturating magnetic field of 1T applied in the plane of the device, *i.e.*, in the pure AMR geometry with zero (antisymmetric) Hall signal. Magnetometry measurements were carried out using a commercial Quantum Design SQUID magnetometer.

Figures 1(a) and (b) show the fractional change in the resistivity, $\Delta\rho_{xx}/\rho_{av}$ and $\Delta\rho_{xy}/\rho_{av}$ ($\Delta\rho_{xx} = \rho_{xx} - \rho_{av}$) for the Hall bars fabricated from the 25nm film for each current direction. Here ρ_{av} is the average value of the longitudinal resistance as the magnetic field is rotated through 360°. In the following analysis we will show that this data can be decomposed into the form given by equations (1) and (2). In the subsequent sections we aim to identify the origin of the particular contributions.

The terms allowed by symmetry are obtained by extending the standard phenomenology [2], to systems with cubic [100] plus uniaxial [110] anisotropy:

$$\frac{\Delta\rho_{xx}}{\rho_{av}} = C_I \cos 2\phi + C_U \cos 2\psi + C_C \cos 4\psi + C_{I,C} \cos(4\psi - 2\phi) \ . \qquad (1)$$

$$\frac{\Delta\rho_{xy}}{\rho_{av}} = C_I \sin 2\phi - C_{I,C} \sin(4\psi - 2\phi) \ . \qquad (2)$$

ϕ is the angle between the magnetization unit vector $\hat{M}$ and the current I, and ψ the angle between $\hat{M}$ and the [110] crystal direction. The four contributions are the non-crystalline term, the lowest order uniaxial and cubic crystalline terms, and a crossed non-crystalline/crystalline term. We have omitted the higher order terms in these expressions as these are found to be negligibly small in our devices. The purely crystalline terms are excluded by symmetry for the transverse AMR and it is clear that $\Delta\rho_{xy}/\rho_{av}$ and $\Delta\rho_{xx}/\rho_{av}$ are not independent. The well known formulae for isotropic materials (see *e.g.* [8]) correspond to $C_I \neq 0$ and all other coefficients set to zero in equations (1,2). Such formulae result also from equations (1,2) averaged over ψ with ϕ held constant, which corresponds to a polycrystal with randomly oriented grains.

It is not possible to obtain each term separately by fitting equations (1) and (2) to the full (ψ) angular data from one Hall bar. In a [1$\bar{1}$0] oriented Hall bar, for instance, $\phi = \psi + \frac{\pi}{2}$, the equations reduce to $\Delta\rho_{xx}/\rho_{av} = (-C_I + C_U - C_{I,C}) \cos 2\psi + C_C \cos 4\psi$ and $\rho_{xy}/\rho_{av} = -C_I + C_{I,C} \sin 2\psi$. C_I and $C_{I,C}$ could be determined only if $C_U = 0$. However, using different Hall bar orientations, the anisotropy constants appear in other combinations so that they can all be extracted individually. In the present case, two Hall bar orientations (e.g. [110] and [1$\bar{1}$0]) suffice. Measurements with other orientations are used as consistency checks.

Figure 2(a) shows some examples of how the individual AMR components can be extracted: the longitudinal resistivities in the [010] and [100] directions are subtracted to give a simple $\sin 2\psi$ signal (cf. Eq. 1) with amplitude $2(C_I - C_{I,C})$ and this is the same as the difference of transverse resistivities in the [110] and [1$\bar{1}$0] samples. A $\cos 2\psi$ signal with amplitude $2(C_I + C_{I,C})$ can be obtained through other combinations of the data. The close agreement obtained by using different combinations to extract the same coefficients highlights the consistency between the data and our phenomenological analysis, and also attests to the homogeneity and quality of the MBE grown GaMnAs wafer.

The purely crystalline terms can be extracted from the combination of the measurements from two orthogonal bars. This is shown in Fig. 2(b) for our data. In principle, the same signals could be extracted directly from a single experimental measurement by appropriate wiring of an *L*-shaped Hall bar. Alternatively, the same coefficients can be extracted directly from the data obtained from the Corbino geometry, Fig. 2(b). As the current flows in all radial directions, the non-crystalline terms are averaged to zero[14]. It would

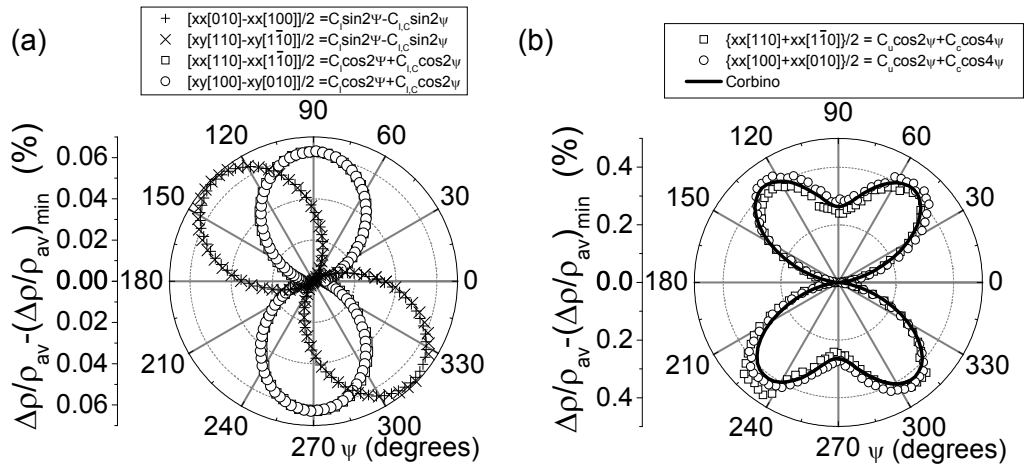

Fig. 2. Combinations of the data from Fig.1 used to extract the AMR components. The notation xx[100] is used to denote $\Delta\rho_{xx}/\rho_{av}$ for current along the [100] direction etc.

be problematic to perform such measurements with ferromagnetic metals because, in order to define the Corbino geometry it is required that the source-drain resistance be large compared to the contact resistances. This condition is met with (Ga,Mn)As. Again, we obtain excellent agreement for the same coefficients extracted from different combinations of devices.

Figure 3(a) shows the coefficients $C_{I,C}$, C_U and C_C extracted from the Hall bar and Corbino disk data over the whole range up to the Curie temperature (80K). Note that the uniaxial crystalline term, C_U, becomes the dominant term for T$\geqslant$30K. This correlates with the uniaxial component of the magnetic anisotropy which dominates for T$\geqslant$30K as observed by SQUID magnetometry measurements (Figure 3(b)). Our work shows that in (Ga,Mn)As ferromagnets, the symmetry breaking mechanism behind this previously reported [15] uniaxial magneto-crystalline anisotropy in the magnetization also contributes to the AMR.

In our previous work [13] we used the techniques explained above to extract the individual AMR components for ultra thin (5nm) $Ga_{0.95}Mn_{0.05}As$ films for which the AMR (Fig. 4(a)) is very different from that observed in the 25nm film. For the 5nm film, the uniaxial crystalline term dominates the AMR as shown in the Fig. 4(b) for the device in the Corbino geometry. These techniques were also used to demonstrate how the crystalline terms can be tuned by the use of lithographic patterning to induce an additional uniaxial anisotropy in very narrow Hall bars. It has been shown [18,19] that the fabrication of narrow bars allows the in-plane compressive strain in the (Ga,Mn)As film to relax in the direction along the width of the Hall bar and this can lead to an additional uniaxial component in the magnetocrystalline anisotropy for bars with widths on the order of 1μm or smaller. Figs. 5(a) and (b) show

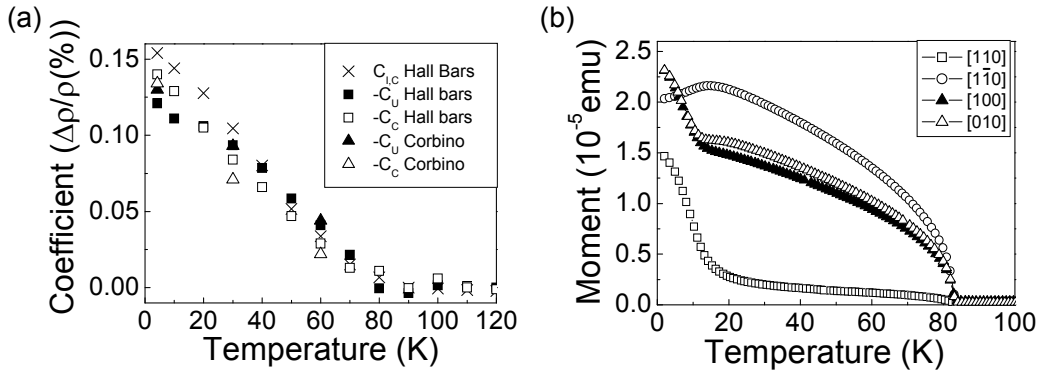

Fig. 3. (a) Temperature dependence of the crystalline terms extracted from the Hall bars and Corbino devices. (b) Remnant moment of 25nm $Ga_{0.95}Mn_{0.05}As$ film measured by SQUID magnetometer along different crystalline directions after cooling in a field of 0.1T.

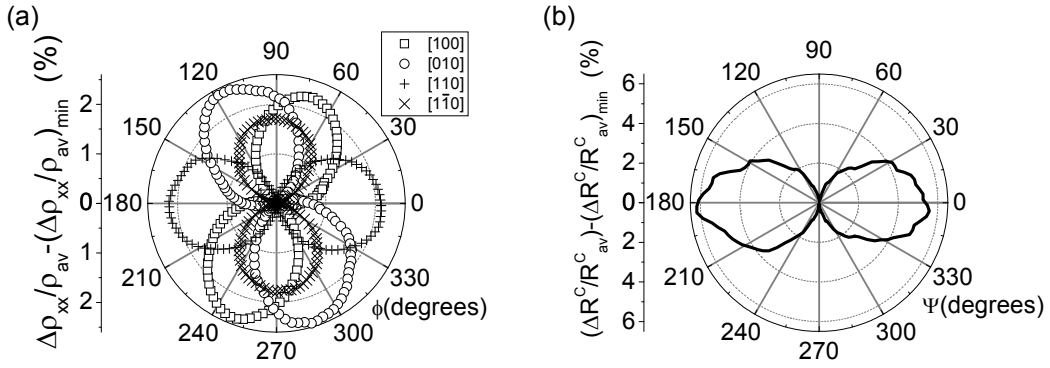

Fig. 4. Longitudinal AMR of the 5nm $Ga_{0.95}Mn_{0.05}As$ Hall bars. T=20K. (b) AMR of a 5nm $Ga_{0.95}Mn_{0.05}As$ film in the Corbino geometry. T=11K.

the AMR of 45μm wide bars and 1μm wide bars fabricated from nominally identical 25nm $Ga_{0.95}Mn_{0.05}As$ wafers. For the 45μm bars, the cubic crystalline symmetry leads to the AMR along [100] and [010] being larger than along [110] and [1$\bar{1}$0]. For the narrow bars we observe the opposite relationship, consistent with the addition of an extra uniaxial component which adds 0.8% to the AMR when current is along [110] and [1$\bar{1}$0] and subtracts 0.4% when the current is along [100] and [010].

It is anticipated that the experimental techniques developed here will be useful in studying the magnetotransport coefficients in other magnetic materials and nanostructures.

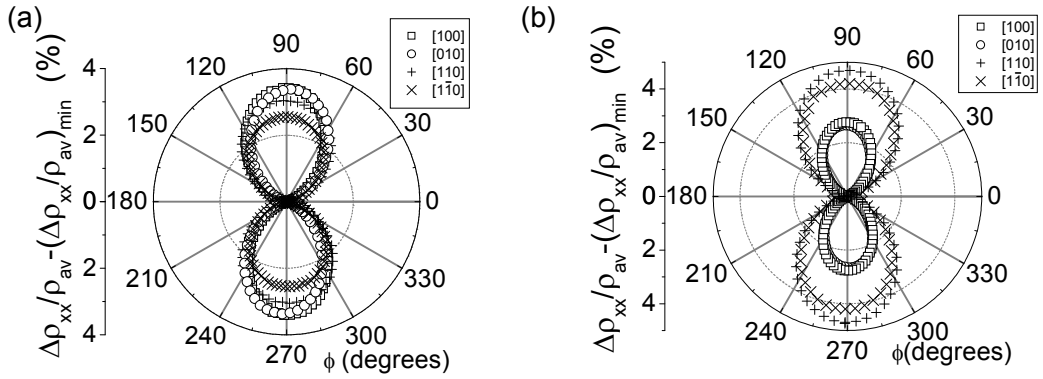

Fig. 5. (a) AMR for macroscopic Hall bars and (b) narrow (1μm wide) Hall bars fabricated from 25nm $Ga_{0.95}Mn_{0.05}As$ films. T=4.2K.

3 From the full Boltzmann theory simulations to a simple analytical model of the AMR

A six-band $\vec{k}\cdot\vec{p}$ description of the GaAs host valence band combined with the kinetic-exchange model of the coupling to the local Mn_{Ga} d^5-moments [20] can provide input for the Boltzmann equation producing the conductivity tensor σ. In our previous work [13], we expanded the studies of Jungwirth *et al.* [23,7] by performing numerical calculations of the σ_{xx} for arbitrary in-plane directions of $\hat{M}$ (not just $\hat{M}||I$ and $\hat{M}\perp I$). The results of the calculations (see Fig. 6) are in semi-quantitative agreement with the experimental AMRs for the 25nm $Ga_{0.95}Mn_{0.05}As$ films shown in Fig. 1 (a,b). The zero-temperature model of a 15% compensated material [24] shows that both the $\Delta\rho_{xx}/\rho_{\rm av}$ and $\Delta\rho_{xy}/\rho_{\rm av}$ are dominated by the non-crystalline $\cos 2\phi$ and $\sin 2\phi$ part, being of the order of several percent and negative ($C_I=-2.2\%$). The crystalline terms are an order of magnitude smaller ($C_U=-0.2\%$, $|C_C|<0.1\%$, $C_{I,C}=0.4\%$). These calculations assumed a growth strain $e_0=-0.3\%$ and a uniaxial strain [21] $e_{xy}=-0.01\%$.

Previously, we noted that the crystalline terms arise from the warping of the valence band [13]. In the rest of this paper we concentrate only on the non-crystalline component of the AMR (C_I) which in our model originates from anisotropic scattering of spin-orbit coupled holes on Mn_{Ga} impurities containing polarized local moments.

The six-band Kohn-Luttinger Hamiltonian H_{KL} is parameterized by the Luttinger parameters $\gamma_1,\gamma_2,\gamma_3$ and SO splitting Δ_{SO} while the exchange splitting strength is characterized by the constant J_{pd} [20]. The total Hamiltonian then reads

$$H=H_{KL}+J_{pd}\sum_{i,I}\vec{S}_I\cdot\vec{s}_i\delta(\vec{r}_i-\vec{R}_I)\,, \tag{3}$$

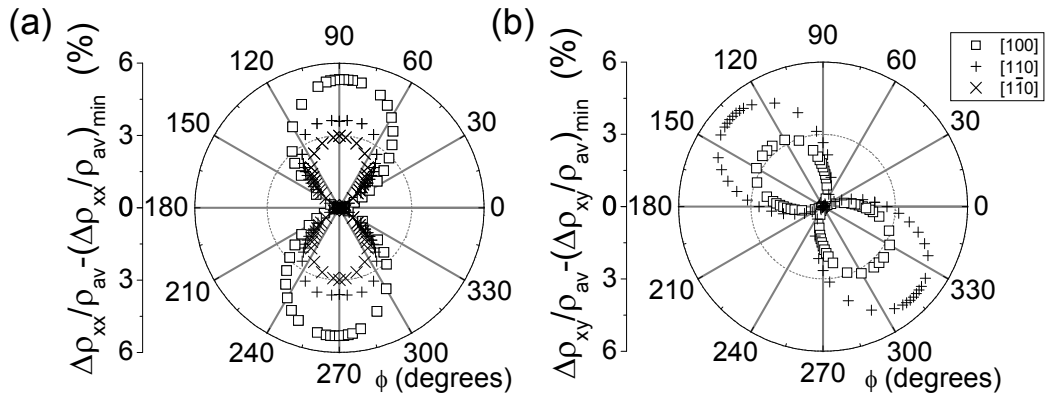

Fig. 6. Calculated angular dependence of the AMR (see the text for system parameters).

where $\vec{S}_I$ and $\vec{s}_i$ denote the Mn and hole spins placed at $\vec{r}_i$ and $\vec{R}_I$. The mean-field treatment of the exchange splitting (second term in Eq. (3)) leads to a term formally equivalent to an effective Zeeman splitting of strength $h = J_{pd} N_{\rm Mn} S_{\rm Mn}$, where $N_{\rm Mn}$ is the Mn concentration and $S_{\rm Mn} = \frac{5}{2}$ for the five Mn d-electrons. In the following we consider the spherical approximation to H_{KL} ($\gamma_2 = \gamma_3$) and the four-band model ($\Delta_{SO} \to \infty$). The total Hamiltonian can be then rewritten as

$$H = (\gamma_1 + \tfrac{5}{2}\gamma_2)\hbar^2 k^2/2m - 2\gamma_2(\vec{k}\cdot\vec{J})^2\hbar^2/2m + h\hat{M}\cdot\vec{s}\,. \tag{4}$$

Explicit expressions of the matrices for the total angular momentum $\vec{J}$ and hole spin $\vec{s}$ can be found in Refs. [26] and [22]. With this simplified band structure we will now estimate the AMR assuming that the scattering takes place only on Mn ions substituting Ga which is the dominant mechanism.

Numerically, the light hole bands are found to give only small contribution to the total conductivity as shown in Fig. (7), hence we consider only the heavy hole bands. This is a substantial simplification since the Hamiltonian (4) restricted to the heavy-hole subspace $j_k = \pm\frac{3}{2}$ can be diagonalized analytically (see Appendix A). By denoting the angle between $\vec{k}$ and $\hat{M}$ as $\phi_{\vec{k}}$ the eigenenergies read

$$E_{1,2} = (\gamma_1 - 2\gamma_2)\hbar^2 k^2/2m \pm h\cos\phi_{\vec{k}}\,. \tag{5}$$

In the presence of the exchange field h the two originally identical heavy-hole Fermi spheres transform into (typically weakly) distorted '+' and '−' spheres displaced by $\Delta k = \pm(2m_*/\hbar)^{1/2}h/4\sqrt{E_F}$ along $\hat{M}$. The eigenstates $|hh+\vec{k}\rangle$, $|hh-\vec{k}\rangle$ are independent of h and correspond to perfectly isotropic radial spin textures: expectation value of $\vec{s}$ in the state $|hh+\vec{k}\rangle$ ($|hh-\vec{k}\rangle$) is a vector

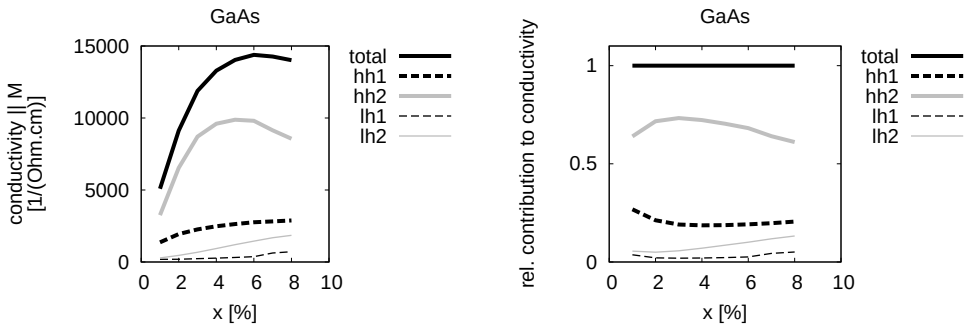

Fig. 7. Contribution of particular bands to the calculated total bulk conductivity in uncompensated GaAs. (a) Absolute values, (b) relative to the total conductivity.

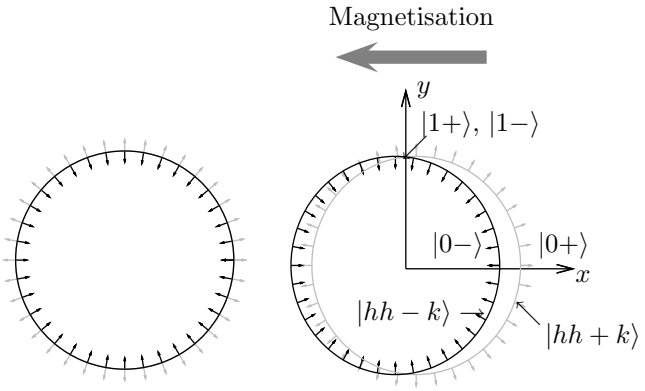

Fig. 8. Heavy hole bands. Spin texture without and with exchange splitting.

of length $\frac{1}{2}$ parallel to $\vec{k}$ and pointing outwards (inwards), Fig. 8. We remark that Eq. (5) and $|hh \pm \vec{k}\rangle$ remain unchanged even when the Hamiltonian (5) is extended to include a finite Δ_{SO} (see Appendix A).

In the lowest order Born approximation, the transport relaxation time is given by

$$\frac{1}{\tau(\vec{k})} = \int \frac{d^3\vec{k}'}{(2\pi)^3}\frac{2\pi}{\hbar} N_{\mathrm{Mn}} \delta(E(\vec{k}) - E(\vec{k}'))|M_{\vec{k}\vec{k}'}|^2(1 - \hat{k}\cdot\hat{k}')\,. \tag{6}$$

The last factor corresponds to vertex corrections in the Kubo formalism and $\hat{k}\cdot\hat{k}'$ is the cosine of the angle between $\vec{k}$ and $\vec{k}'$. The scattering matrix element between initial $|z_{\vec{k}'}\rangle$ and final $|z_{\vec{k}}\rangle$ states is

$$M^C_{\vec{k}\vec{k}'} = \langle z_{\vec{k}}|V(\vec{k} - \vec{k}')|z_{\vec{k}'}\rangle = V(|\vec{k} - \vec{k}'|)\langle z_{\vec{k}}|z_{\vec{k}'}\rangle \tag{7}$$

for the isotropic (e.g. screened Coulomb) scattering off a charged ion, and

$$M^B_{\vec{k}\vec{k}'} = \langle z_{\vec{k}}|(h/N_{\rm Mn})\hat{M}\cdot\vec{s}|z_{\vec{k}'}\rangle = J_{pd}S_{\rm Mn}\langle z_{\vec{k}}|\hat{M}\cdot\vec{s}|z_{\vec{k}'}\rangle \tag{8}$$

for the scattering off a magnetic moment. These two add up coherently for substitutional Mn so that $M_{\vec{k}\vec{k}'} = M^B_{\vec{k}\vec{k}'} + M^C_{\vec{k}\vec{k}'}$.

To simplify the further qualitative analytical discussion we replace the long-range Coulomb potential with an effective δ-function potential and denote the ratio of this non-magnetic potential and of $J_{pd}S_{Mn}$ as α. Our relaxation rates will be evaluated from the following scattering operator

$$M_{\vec{k}\vec{k}'} \propto \langle z_{\vec{k}}|\alpha + s_x|z_{\vec{k}'}\rangle\,. \tag{9}$$

We discarded an overall prefactor, since when only one source of scattering is present, this prefactor will cancel in the expressions for relative changes of conductivity needed to obtain the AMR.

Equation (6) will now be used to calculate the scattering rates for two special values of $\vec{k}$, details of that calculation are given in Appendix B. The first one is $\vec{k}||\hat{M} = \hat{e}_x$. The corresponding initial states for the scattering, $|hh\pm\vec{k}\rangle$ will be abbreviated as $|0\pm\rangle$, see Fig. 8. Integrands in Eq. (6) can be simplified considerably noting that $s_x|0\pm\rangle = \pm\frac{1}{2}|0\pm\rangle$. We obtain

$$\begin{aligned}\frac{1}{\tau^x_\pm} = \int\limits_{FS} d^2\vec{k}' \Big\{ &|\langle hh+\vec{k}'|0\pm\rangle|^2(\alpha\pm\frac{1}{2})^2 + \\ &+|\langle hh-\vec{k}'|0\pm\rangle|^2(\alpha\pm\frac{1}{2})^2\Big\}(1-\hat{k}\cdot\hat{k}')\,.\end{aligned} \tag{10}$$

The integration variable is taken as dimensionless and the result should be multiplied by a factor $R = 2mk_F/h^2\cdot 2\pi/\hbar\cdot N_{\rm Mn}\cdot(J_{pd}S_{\rm Mn})^2$ to get the real inverse scattering times based on Eqs. (7,8) with $V(\vec{k}-\vec{k}') \equiv \alpha J_{pd}S_{\rm Mn}$. By integrating Eq. (10) we obtain,

$$1/\tau^x_+ = 2\pi(\alpha-\tfrac{1}{2})^2 \qquad 1/\tau^x_- = 2\pi(\alpha+\tfrac{1}{2})^2\,.$$

In contrast, the other pair of initial states $|1\pm\rangle$ with $\vec{k}\perp\hat{M}$ (see Fig. 8), gives

$$\begin{aligned}\frac{1}{\tau^y_\pm} = \int\limits_{FS} d^2\vec{k}' \Big\{ &|\langle hh+\vec{k}'|1\pm\rangle|^2\alpha^2 + |\langle hh+\vec{k}'|s_x|1\pm\rangle|^2 + \\ &|\langle hh-\vec{k}'|1\pm\rangle|^2\alpha^2 + |\langle hh-\vec{k}'|s_x|1\pm\rangle|^2\Big\}(1-\hat{k}\cdot\hat{k}')\,.\end{aligned} \tag{11}$$

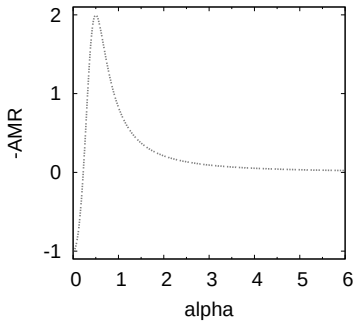

Fig. 9. AMR as a function of the ratio between effective strengths of the non-magnetic and magnetic scattering.

The integrals not involving s_x give again 2π by the virtue of symmetry (cf. Eq. (10) and Fig. 8) while the remaining two terms have to be evaluated independently to give

$$1/\tau_+^y = 1/\tau_-^y = 2\pi(\alpha^2 + \frac{1}{12}) \tag{12}$$

Conductivities for $\hat{M}||I$ and $\hat{M} \perp I$ can be estimated based on these relaxation rates as $\sigma_{||} = P(\tau_+^x + \tau_-^x)$ and $\sigma_\perp = P(\tau_+^y + \tau_-^y)$, i.e.

$$\sigma_{||}/P = \frac{1}{(\alpha - \frac{1}{2})^2} + \frac{1}{(\alpha + \frac{1}{2})^2} \qquad \sigma_\perp/P = \frac{2}{\alpha^2 + \frac{1}{12}}\,, \tag{13}$$

where $P = e^2 v_F^2/3 \cdot gR/2\pi$, v_F is the Fermi velocity and g is the density of states at the Fermi wavevector k_F. For heavy holes, $v_F = (\gamma_1 - 2\gamma_2)\hbar k_F/m$ and $g = 2mk_F/h^2(\gamma_1 - 2\gamma_2)$. Eq. (13) leads to

$$\frac{\sigma_{||}}{\sigma_\perp} = \frac{(\alpha^2 + \frac{1}{12})(\alpha^2 + \frac{1}{4})}{(\alpha^2 - \frac{1}{4})^2}\,, \tag{14}$$

presented in Ref. [13]. The AMR, using the notation of the experimental section then reads

$$\mathrm{AMR} = 2\frac{\rho_{xx}(\hat{M}||I) - \rho_{xx}(\hat{M} \perp I)}{\rho_{xx}(\hat{M}||I) + \rho_{xx}(\hat{M} \perp I)} = -2\frac{\sigma_{||} - \sigma_\perp}{\sigma_{||} + \sigma_\perp} = -\frac{20\alpha^2 - 1}{24\alpha^4 - 2\alpha^2 + 1}\,. \tag{15}$$

When the magnetic term in the impurity potential is much larger than the non-magnetic term ($\alpha \ll 1$) one expects $\sigma_\parallel < \sigma_\perp$ (positive AMR, as is usually observed in metallic ferromagnets). However, the sign of the non-crystalline AMR reverses at a relatively weak non-magnetic potential ($\alpha = 1/\sqrt{20}$ in the model), its magnitude is then maximized when the two terms are comparable

($\alpha = 1/2$), and, for this mechanism, it vanishes when the magnetic term is much weaker than the non-magnetic term ($\alpha \to \infty$). Note that the large magnitude of the AMR for $\alpha = 1/2$ due to $1/\sigma_{\|} = 0$ is an artefact of the special form of the simplified scattering operator (9) where the magnetic and non-magnetic part depend in exactly the same way on k (they are constant, i.e. they both correspond to point-like scatterers).

Physically, carriers moving along $\hat{M}$, *i.e.* with $\vec{s}$ parallel or antiparallel to $\hat{M}$, experience the strongest scattering potential among all Fermi surface states when $\alpha = 0$, giving $\sigma_{\|} < \sigma_{\perp}$. When the non-magnetic potential is present, however, it can more efficiently cancel the magnetic term for carriers moving along $\hat{M}$, and for relatively small α the sign of AMR flips. Since $\alpha < 1/\sqrt{20}$ is unrealistic for the magnetic acceptor Mn in GaAs [23,17] we obtain $\sigma_{\|} > \sigma_{\perp}$, consistent with experiment.

4 Summary

A phenomenological framework for the AMR in the zinc-blende crystalline environment of GaMnAs was used to analyse experimental data from (i) bulk material, (ii) thin layers, and (iii) samples with lithographically manipulated strain. While leaving the crystalline components aside for a further theoretical study, a qualitative analytical model was presented for the non-crystalline AMR. The model is based on the anisotropic relaxation times in the heavy hole bands due to a combined magnetic/non-magnetic scattering on Mn impurities. It offers an explanation of the sign of the non-crystalline AMR in GaMnAs which is opposite to most of the conventional metal ferromagnets.

We acknowledge support from EU Grant IST-015728, from UK Grant GR/S81407/01, from CR Grants 202/05/0575, 202/04/1519, FON/06/E002, AV0Z1010052, KAN400100652, and LC510, from ONR Grant N000140610122, and from SWAN. J. Sinova is a Cottrell Scholar of Research Corporation.

A Some basic algebra with Kohn–Luttinger Hamiltonian

Equation (5) and explicit form of the heavy-hole eigenvectors $|hh \pm \vec{k}\rangle$ will be derived in this Appendix. As we will refer to the spherical approximation with $\hat{M}||\hat{e}_x$, the main body of calculations will be carried out in the k_x, k_y plane keeping in mind the rotational symmetry of the problem around $\hat{e}_x$. For the sake of completeness, results for general $k_z \neq 0$ will be given at the end of each part without derivation.

The starting point is H_{KL} as in Eq. (A8) of Abolfath *et al.*[22]

$$H_{KL} = \begin{pmatrix} H_{hh} & -c & -b & 0 & b/\sqrt{2} & c\sqrt{2} \\ -c^* & H_{lh} & 0 & b & -b^*\sqrt{3}/\sqrt{2} & -d \\ -b^* & 0 & H_{lh} & -c & d & -b\sqrt{3}/\sqrt{2} \\ 0 & b^* & -c^* & H_{hh} & -c^*\sqrt{2} & b^*/\sqrt{2} \\ b^*/\sqrt{2} & -b\sqrt{3}/\sqrt{2} & d^* & -c\sqrt{2} & H_{so} & 0 \\ c^*\sqrt{2} & -d^* & -b^*\sqrt{3}/\sqrt{2} & b/\sqrt{2} & 0 & H_{so} \end{pmatrix} . \quad \text{(A.1)}$$

Going into the k_x, k_y plane by putting $\vec{k} = k(\cos\phi, \sin\phi, 0)$, the off-diagonal elements become

$$b = 0\,, \qquad c = \frac{\sqrt{3}\hbar^2 k^2}{2m}[\gamma_2 \cos 2\phi - i\gamma_3 \sin 2\phi]\,, \qquad d = \frac{\sqrt{2}\hbar^2 k^2}{2m}\gamma_2\,,$$

and the diagonal elements are independent of ϕ

$$H_{hh} = \frac{\hbar^2 k^2}{2m}(\gamma_1 + \gamma_2)\,, \qquad H_{lh} = \frac{\hbar^2 k^2}{2m}(\gamma_1 - \gamma_2)\,, \qquad H_{so} = \frac{\hbar^2 k^2}{2m}\gamma_1 + \Delta_{SO}\,.$$

It is convenient to factor out $\hbar^2 k^2/(2m)$ and to introduce $\delta = \Delta_{SO}/(\gamma_2\hbar^2/2m)\cdot k^{-2}$.

The spherical approximation relies in setting $\gamma_2 = \gamma_3$ and allows for the simplification

$$c/(\hbar^2 k^2/(2m)) = \sqrt{3}\gamma_2 \exp(-2i\phi)\,.$$

In this approximation and even with general $k_z \neq 0$, i.e.

$$\vec{k} = k(\sin\theta\cos\phi, \sin\theta\sin\phi, \cos\theta) \quad \text{(A.2)}$$

the spectrum of the Hamiltonian (A.1) does not depend on θ, ϕ. Below, this statement is demonstrated explicitly for $\theta = \pi/2$.

A.1 Spectrum

When $k_z = 0$, rows/columns 3,4,5 of H_{KL} are totally decoupled from rows/columns 1,2,6. The 6×6 problem is reduced to two independent and equivalent 3×3

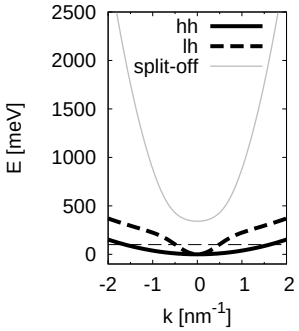

Fig. A.1. Dispersions of the heavy holes, light holes and the split-off band in the spherical approximation. Horizontal dashed line indicates the Fermi energy of E_F =100meV.

problems. The latter (lines 1,2,6) is

$$A_+ = H/(\hbar^2 k^2/2m) = \begin{pmatrix} \gamma_1+\gamma_2 & -c & c\sqrt{2} \\ -c^* & \gamma_1-\gamma_2 & -\sqrt{2}\gamma_2 \\ \sqrt{2}c^* & -\sqrt{2}\gamma_2 & \gamma_1+\gamma_2\delta \end{pmatrix} . \tag{A.3}$$

Matrix A_+ depends on ϕ only via c. In the spherical approximation, $cc^* = |c|^2 = 3\gamma_2^2$ is ϕ-independent. The eigenvalues of A_+ are calculated from $\det(A_+ - \lambda) = 0$. This determinant will depend on c only via the combination cc^* and hence it is ϕ-independent for $\gamma_2 = \gamma_3$.

Explicitly, Fig. A.1, the eigenvalues of A_+, multiplied back by $\hbar^2k^2/2m$, are

$$\begin{aligned} E_1 &= \frac{\hbar^2k^2}{2m}\left[\gamma_1 - 2\gamma_2\right] \\ E_2 &= \frac{\hbar^2k^2}{2m}\left[\gamma_1 + \gamma_2 \cdot \frac{1}{2}(\delta + 2 - \sqrt{\delta^2 - 4\delta + 36})\right] \\ E_3 &= \frac{\hbar^2k^2}{2m}\left[\gamma_1 + \gamma_2 \cdot \frac{1}{2}(\delta + 2 + \sqrt{\delta^2 - 4\delta + 36})\right] . \end{aligned} \tag{A.4}$$

They correspond to heavy holes, light holes and the split-off band, the last two depend on k via δ, but none of them depends on ϕ and hence give circular FS sections. The light-hole energy is $[\gamma_1 + 2\gamma_2]\hbar^2k^2/(2m)$ in the limit $\Delta_{SO} \to \infty$.

Analysis of the complete Hamiltonian H_{KL} is completed by constructing matrix A_- from lines 3,4,5. It is not identical to A_+, but it has an identical spectrum to A_+. Thus, the Fermi surfaces of H_{KL} in the $k_z = 0$ sections comprise of, largest to smallest, two coincident circles for heavy holes with $E_F = (\gamma_1 - 2\gamma_2)\hbar^2k_F^2/2m$, which is independent of Δ_{SO}, two coincident circles for light holes and two coincident circles for split-off bands.

A.2 Eigenvectors

Even though the spectrum of the Hamiltonians (A.1) or (A.3) does not depend on ϕ, θ, the eigenvectors do.

The lowest-energy ($E_1 = \gamma_1 - 2\gamma_2$) eigenvector of A_+ is independent of δ. Together with its counterpart from A_- they represent the degenerate heavy-hole states of H_{KL} regardless of Δ_{SO}:

$$\vec{v}_{1+} = \frac{1}{2}(e^{-2i\phi}, \sqrt{3}, 0, 0, 0, 0)^T\,, \qquad \vec{v}_{1-} = \frac{1}{2}(0, 0, \sqrt{3}, e^{2i\phi}, 0, 0)^T\,.$$

The component notation refers to the basis (A5) of Ref. [22], the superscript denotes the transposition. For a general $\vec{k}$ given by Eq. (A.2) the heavy-hole states are

$$\vec{v}_{1+} = \frac{1}{2}(e^{-2i\phi}\sin\theta, \sqrt{3}\sin\theta, 0, -e^{i\phi}\cos\theta, 0, 0)^T\,,$$

$$\vec{v}_{1-} = \frac{1}{2}(e^{-i\phi}\cos\theta, 0, \sqrt{3}\sin\theta, e^{2i\phi}\sin\theta, 0, 0)^T\,.$$

A.3 Perturbation theory with kinetic exchange

The p-d kinetic exchange has the form of an effective Zeeman field in the magnetisation direction which we choose to be x, Fig. 8. The corresponding operator (with respect to the first four basis vectors of (A5) in Ref. [22]), that is the last term in Eq. (4), is

$$H_{pd} = hs_x = h\frac{1}{6}\begin{pmatrix} 0 & 0 & \sqrt{3} & 0 \\ 0 & 0 & 2 & \sqrt{3} \\ \sqrt{3} & 2 & 0 & 0 \\ 0 & \sqrt{3} & 0 & 0 \end{pmatrix}. \tag{A.5}$$

The matrix of H_{pd}/h in the basis of $\vec{v}_{1+}$, $\vec{v}_{1-}$ and its diagonalization results are the following

$$H_{pd}/h = \frac{1}{4}\begin{pmatrix} 0 & 1+e^{2i\phi} \\ 1+e^{-2i\phi} & 0 \end{pmatrix}, \qquad \begin{aligned} E_+ &= \tfrac{1}{2}\cos\phi\,, \quad \vec{v}_+ = 2^{-1/2}(1, e^{-i\phi})^T \\ E_- &= -\tfrac{1}{2}\cos\phi\,, \quad \vec{v}_- = 2^{-1/2}(1, -e^{-i\phi})^T\,. \end{aligned}$$

In the limit of small h ('degenerate-level perturbation calculus') the degenerate heavy-hole bands of H_{KL} become split in energy by $h\cos\phi$. Recast into the $\vec{k}$-

plane, the two coincident Fermi circles become displaced. Their wavefunctions are

$$|hh+,\vec{k}\rangle = \frac{1}{2\sqrt{2}}(e^{-2i\phi}, \sqrt{3}, \sqrt{3}e^{-i\phi}, e^{i\phi}, 0, 0)^T\,, \tag{A.6}$$
$$|hh-,\vec{k}\rangle = \frac{1}{2\sqrt{2}}(e^{-2i\phi}, \sqrt{3}, -\sqrt{3}e^{-i\phi}, -e^{i\phi}, 0, 0)^T\,.$$

For general $k_z \neq 0$ (A.2) the energies are

$$E_\pm = \pm\frac{1}{2}\cos\phi\sin\theta\,,$$

as stated in Eq. (5), and the eigenvectors

$$|hh+,\vec{k}\rangle = (e^{-2i\phi}C^3, \sqrt{3}CS^2, \sqrt{3}e^{-i\phi}C^2S, e^{i\phi}S^3, 0, 0)^T\,, \tag{A.7}$$
$$|hh-,\vec{k}\rangle = (e^{-2i\phi}S^3, \sqrt{3}SC^2, -\sqrt{3}e^{-i\phi}S^2C, -e^{i\phi}C^3, 0, 0)^T$$

with $C = \cos\theta/2$ and $S = \sin\theta/2$.

B Integrals of overlaps, Eqs. (10,11)

The overlaps of eigenvectors in Eq. (A.6) are

$$\langle hh+\vec{k}|hh+\vec{k}'\rangle = \frac{1}{8}[(e^{2i(\phi-\phi')}+3) + e^{i(\phi-\phi')}(e^{-2i(\phi-\phi')}+3)]\,,$$
$$\langle hh-\vec{k}|hh+\vec{k}'\rangle = \frac{1}{8}[(e^{2i(\phi-\phi')}+3) - e^{i(\phi-\phi')}(e^{-2i(\phi-\phi')}+3)]\,.$$

Note that these overlaps for $J = \frac{3}{2}$ spinors are not the same as for $J = \frac{1}{2}$ spinors $|a \pm \vec{k}\rangle = (1, \pm e^{i\phi})^T$ even though the spin textures of $|hh \pm \vec{k}\rangle$ and $|a \pm \vec{k}\rangle$ are the same, Fig. 8.

The two summands of integral in Eq. (10),

$$\int_{FS} d^2\vec{k}'|\langle hh+\vec{k}'|0\pm\rangle|^2(1-\hat{k}\cdot\hat{k}') \tag{B.1}$$

will be integrated with spherical coordinates ϕ', Φ' with 'north pole' $\phi' = 0$ in

$\vec{k}'||\hat{e}_x$. The polar angle (Φ') integration gives a factor of 2π and we obtain

$$\frac{2\pi}{64}\int\limits_0^\pi d\phi' \sin\phi' \cdot 2[10 \pm 15\cos\phi' + 6\cos 2\phi' \pm \cos 3\phi'](1-\cos\phi')$$

For the + sign we get $4\pi(6+\frac{2}{5})/64$ and for $-$ it is $4\pi(26-\frac{2}{5})/64$ giving the total of 2π. The integrals with $\langle hh-\vec{k}'|$ in Eq. (B.1) are analogous.

Concerning the integral in Eq. (11), we first have to show that it is indeed equal to the scattering rate

$$\frac{1}{\tau_\pm^y} = \int\limits_{FS} d^2\vec{k}' \left\{ |\langle hh+\vec{k}'|\alpha+s_x|1\pm\rangle|^2 + |\langle hh+\vec{k}'|\alpha+s_x|1\pm\rangle|^2 \right\} (1-\hat{k}\cdot\hat{k}')\,.$$

In order to show this, it suffices to demonstrate that

$$\int\limits_0^{2\pi} d\Phi' \langle hh+\vec{k}'|\alpha|1+\rangle\langle 1+|s_x|hh+\vec{k}'\rangle = 0$$

which holds by the virtue of $\langle hh+\vec{k}'|s_x|1+\rangle \propto e^{i\Phi'}$ and $\langle hh+\vec{k}'|1+\rangle \propto e^{2i\Phi'}$ [27].

Proceeding with Eq. (11), we will use

$$\begin{aligned}
\langle hh+\vec{k}|s_x|hh+\vec{k}'\rangle &= \frac{1}{8}(e^{i\phi}+e^{-i\phi'})[1+\cos(\phi-\phi')] \\
\langle hh-\vec{k}|s_x|hh-\vec{k}'\rangle &= -\langle hh+\vec{k}|s_x|hh+\vec{k}'\rangle \\
\langle hh-\vec{k}|s_x|hh+\vec{k}'\rangle &= -\frac{1}{8}(e^{i\phi}-e^{-i\phi'})[1-\cos(\phi-\phi')] \\
\langle hh+\vec{k}|s_x|hh-\vec{k}'\rangle &= -\langle hh-\vec{k}|s_x|hh+\vec{k}'\rangle
\end{aligned}$$

Here, the proper choice of $\vec{k}$ ($||\hat{e}_y$) amounts to putting $\phi=\frac{\pi}{2}$ and the integral for scattering from $|1+\rangle$ to the + band is

$$\frac{2\pi}{64}\int\limits_{-\pi/2}^{\pi/2} d\phi' \cos\phi'[1+\sin\phi']^2 2(1-\sin\phi')\cdot(1-\sin\phi') = \frac{2\pi}{32}\cdot\frac{13}{120}\,,$$

while the other integral ($\to -$)

$$\frac{2\pi}{64}\int\limits_{-\pi/2}^{\pi/2} d\phi' \cos\phi'[1-\sin\phi']^2 2(1+\sin\phi')\cdot(1-\sin\phi') = \frac{2\pi}{32}\cdot\left(\frac{8}{3}-\frac{13}{120}\right).$$

Their sum is $2\pi\frac{1}{12}$ which completes the proof of Eq. (12).

References

[1] W. Thomson, Proc. Roy. Soc. **8**, 546 (1857).

[2] W. Döring, Ann. Phys. (Leipzig) **424**, 259 (1938).

[3] R. P. van Gorkom, J. Caro, T. M. Klapwijk, and S. Radelaar, Phys. Rev. **B 63**, 134432 (2001).

[4] J. Banhart and H. Ebert, Europhys. Lett. **32**, 517 (1995).

[5] T. McGuire and R. Potter, IEEE Trans. Magn. **11**, 1018 (1975); J. Smit, Physica **17**, 612 (1951).

[6] D. V. Baxter, *et al.*, Phys. Rev. **B 65**, 212407 (2002).

[7] T. Jungwirth, *et al.*, Appl. Phys. Lett. **83**, 320 (2003).

[8] H. X. Tang, R. K. Kawakami, D. D. Awschalom, and M. L. Roukes, Phys. Rev. Lett. **90**, 107201 (2003).

[9] F. Matsukura, M. Sawicki, T. Dietl, D. Chiba, and H. Ohno, Physica **E 21**, 1032 (2004).

[10] S. T. B. Goennenwein, *et al.*, Phys. Rev. **B 71**, 193306 (2005).

[11] K. Y. Wang, *et al.*, Phys. Rev. **B 72**, 085201 (2005).

[12] W. Limmer, *et al.*, Phys. Rev. **B 74**, 205205 (2006).

[13] A. W. Rushforth, *et al.*, Phys. Rev. Lett., **99**, 147207 (2007).

[14] Strictly, in a Corbino geometry we measure $G^C = I/V = (\sigma_{xx}+\sigma_{yy})/2$ and plot $R^C = 1/G^C$. If we note that $\rho_{xy} \ll \rho_{xx}$ to a good approximation $\Delta R^C/R^C_{av} = (\Delta R^H_{[110]} + \Delta R^H_{[1\bar{1}0]})/2R_{av} = C_U\cos 2\psi + C_C\cos 4\psi$ where the superscipts denote measurements on Hall bars or Corbino devices.

[15] M. Sawicki, *et al.*, Phys. Rev. **B 71**, 121302 (2005).

[16] A.W. Rushforth, *et al.*, Phys. Stat. Sol. (c) **3**, 4078 (2006).

[17] T. Jungwirth, J. Sinova, J. Mašek, J. Kučera, and A. H. MacDonald, Rev. Mod. Phys. **78**, 809 (2006).

[18] S. Hümpfner, *et al.*, Appl. Phys. Lett. **90**, 102102 (2007).

[19] J. Wunderlich, *et al.*, Phys. Rev. B **76**, 054424 (2007).

[20] T. Dietl, H. Ohno, and F. Matsukura, Phys. Rev. **B 63**, 195205 (2001); M. Abolfath, T. Jungwirth, J. Brum, and A. H. MacDonald, Phys. Rev. **B 63**, 054418 (2001).

[21] The microscopic origin of the uniaxial symmetry breaking mechanism in the (Ga,Mn)As epilayers is not known, but is modelled by a weak in-plane shear strain [15].

[22] M. Abolfath, T. Jungwirth, J. Brum, and A. H. MacDonald, Phys. Rev. **B 63**, 054418 (2001), `arXiv:cond-mat/0006093`.

[23] T. Jungwirth, M. Abolfath, J. Sinova, J. Kučera, and A. H. MacDonald, Appl. Phys. Lett. **81**, 4029 (2002), `arXiv:cond-mat/0206416`.

[24] Previous studies show that as-grown material with 5% total Mn concentration is expected to be compensated by approximately 15% due to Mn ions which occupy interstitial positions in the lattice [25].

[25] T. Jungwirth,*et al.*, Phys. Rev. **B 72**, 165204 (2005),

[26] A. Dargys, phys. stat. sol. **(b) 241**, 2954 (2004).

[27] To see this, it is easier to take $|1+\rangle$ as $|hh+\vec{k}\rangle$ with $\vec{k}||\hat{e}_z$, that is $\langle 1+| \propto (1,0,0,0)$. Then $\langle 1+|s_x \propto (0,0,1,0)$ and using Eq. (A.7) $\langle 1+|s_x|hh+\vec{k}\rangle \propto e^{i\phi}$. On the other hand, again from Eq. (A.7), $\langle 1+|hh+\vec{k}\rangle \propto e^{-2i\phi}$.